Formation of Second-Generation Nanoclusters on Metal Nanoparticles Driven by Reactant Gases

Franklin Feng Tao,[*,†] Luan Nguyen,[†] Shiran Zhang,[†] Yuanyuan Li,[‡] Yu Tang,[†] Lei Zhang,[§] Anatoly I. Frenkel,[‡] Younan Xia,[§] and Miquel Salmeron[*,||]

[†]Department of Chemical and Petroleum Engineering and Department of Chemistry, University of Kansas, Lawrence, Kansas 66045, United States

[‡]Department of Physics, Yeshiva University, New York, New York 10016, United States

[§]Department of Chemistry, Georgia Institute of Technology, Atlanta, Georgia 30332, United States

[||]Materials Science Division, Lawrence Berkeley National Lab, Berkeley, California 94720, United States

S *Supporting Information*

ABSTRACT: Heterogeneous catalysis occurs at the interface between a solid catalyst and the reactants. The structure of metal catalyst nanoparticles at the metal–gas interface is a key factor that determines catalytic selectivity and activity. Here we report that second-generation nanoclusters are formed on the initial catalyst nanoparticles as a result of interaction with the reactant molecules when the nanoparticles are in a gas phase at Torr pressure or higher. The formation of the second-generation nanoclusters is manifested by a decrease of the average coordination number of the metal atoms and a shift of their core level energies in the presence of gases. The formation of second-generation nanoclusters increases the number of undercoordinated sites, which are the most active for catalysis in many cases.

Formation of second-generation nanoclusters on metal nanoparticles of catalyst in reactant gases
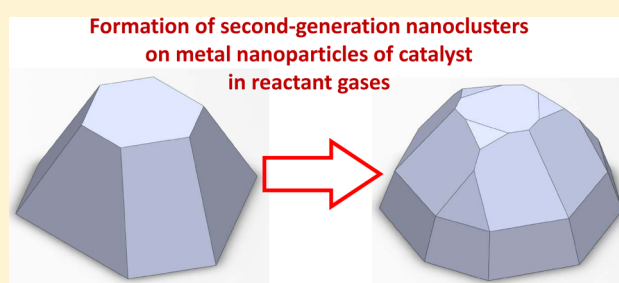
An industrial metal catalyst typically consists of nanoparticles with different shapes and sizes in the range of 1–10 nm or even 1–100 nm, normally supported on an oxide.[1−3] A catalytic active site typically consists of one or a few metal atoms with a specific geometric and electronic structure on the catalyst surface.[4−9] Atomic-scale structure of metal nanoparticles of catalysts is key for understanding catalytic mechanism at a molecular level.[10−13] Resolving the atomic packing of a surface during a catalytic reaction has been challenging in the past due to limitations in the operational capabilities of the surface-sensitive analytical techniques in a gas phase, most of which only work in high vacuum. The advances in development of new surface analytical techniques in recent years has now made such studies feasible.[10,14−16] Here we used lab-based ambient pressure X-ray photoelectron spectroscopy (AP-XPS) and extended X-ray absorption fine structure spectroscopy (EXAFS)[17−20] to study the surface structure of Pd and Pt nanoparticles supported on different oxides and explore their structural evolutions in the presence of reactive gases such as CO, O_2, NO, and H_2. These studies demonstrated the restructuring of these high surface-area metal nanoparticles in reactant gases through the formation of second-generation nanoclusters on their surfaces for the first time.

Results and Discussion. Pd nanoparticles supported on alumina were prepared with a method similar to the one reported in the literature[21] using a NiAl (111) single crystal as a substrate. A STM image of the clean NiAl (111) surface is shown in Figure S1a. Annealing this crystal under O_2 at 600 °C formed an Al_2O_3 film with a thickness of 2–3 nm. The Al_2O_3 film is used to model the inert support commonly used for metal nanoparticles in industry. Its flatness and thickness make it possible to acquire high-resolution scanning tunneling microscopy (STM) images. It has also enough electrical conductivity for XPS studies without surface charging (Figure S2). The atomic scale structure of the Al_2O_3 film was revealed by STM (Figure S1b). The Pd nanoparticles, prepared by electron-beam evaporation of the metal onto the Al_2O_3/NiAl substrate with a precise control of the flux of metal atoms, had an average size of about 3 nm (Figure S1c). The atomic packing of the Pd atoms in the nanoparticle's topmost layer can be clearly observed with STM (Figure S1d).

The chemical states of the Pd NPs/Al_2O_3/NiAl at room temperature in UHV and in the presence of CO gas at different pressures were examined using AP-XPS.[17,22] The Pd $3d_{5/2}$ peak in UHV is located at 335.2 eV (Figure 1a1). At 3×10^{-9} Torr of CO, a shoulder appears on the high binding energy (BE) side of the 335.2 eV peak of the clean surface. The shoulder is marked with red dash line in Figure 1a. Its intensity increases as
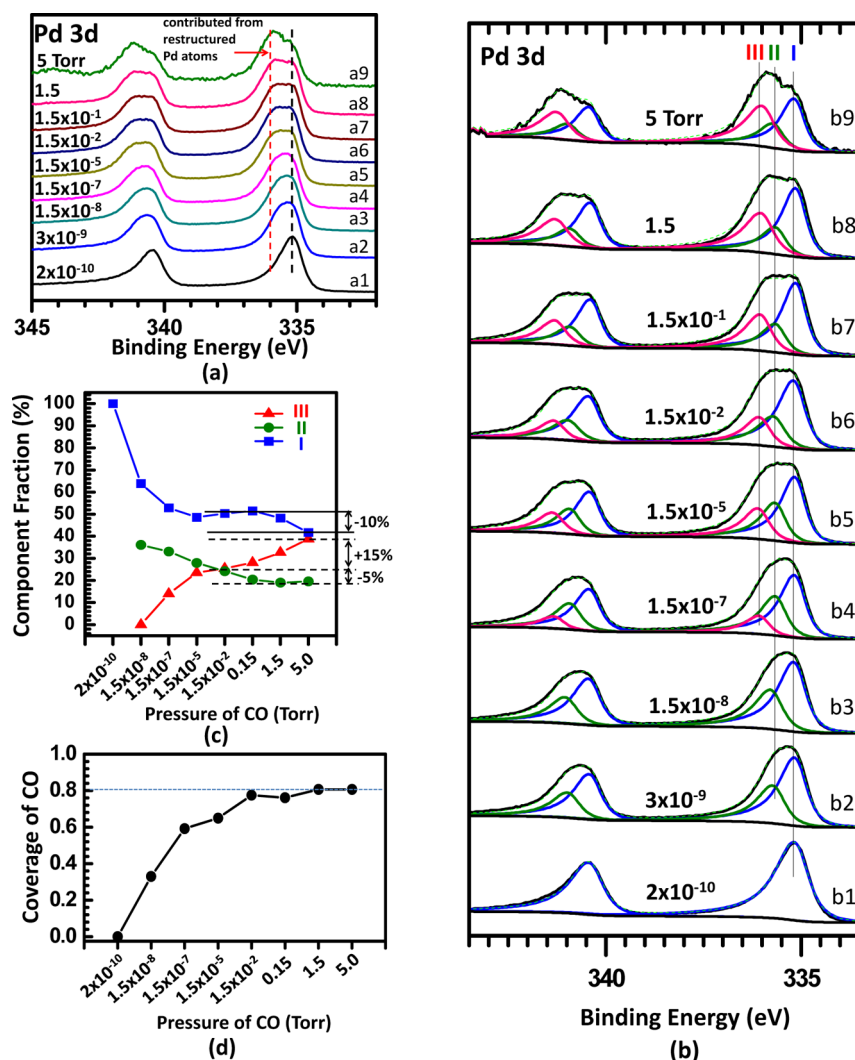
Figure 1. Pressure dependence of photoemission feature of Pd 3d of Pd NPs/Al₂O₃/NiAl in UHV and CO gas with different pressures. (a) Original data of Pd 3d in the pressure range of 2×10^{-10} and 5 Torr. (b) Deconvoluted Pd 3d collected at different pressures of CO; three components I, II, and III, are attributed to Pd atoms of subsurface, Pd atoms (with original coordination number of 9) adsorbing CO molecules, and Pd atoms (with lower coordination number) adsorbing CO molecules; the experimental spectra and fitted curve were shown in black solid line and green dashed line, respectively. (c) Plot of fractions of components I, II and III, as a function of CO pressure. (d) Plot of absolute coverage of CO as a function of CO pressure; here the coverage is defined to the ratio of the number of the chemisorbed CO molecules to the number of Pd atoms in the topmost surface layer of Pd NPs.

a function of CO pressure. At 5 Torr of CO (Figure 1a9), the shoulder marked with red dashed line is more intense than the peak at 335.2 eV. The appearance of the shoulder is neither caused by surface charging, nor due to inelastic scattering effects of the photoelectrons through the gas phase.[17] Broadening caused by any of these effects would also produce a similar effect on the Al 2s photoemission peak which, as shown in Figure S2, is not observed. A similar high BE peak of the Pd 3d level with adsorbed high CO coverage was observed previously and assigned to a new binding sites formed at high coverage.[23] In addition, in our previous study of the effects of CO gas on stepped Pt single-crystal model catalyst, a similar high BE shoulder in the Pt 4f photoemission feature was observed and assigned to the contribution of under-coordinated Pt atoms with adsorbed CO molecules.[13] Similarly, here we can attribute the appearance of the high BE shoulder of Pd 3d to the formation of Pd atoms with lower coordination numbers, induced by CO. These sites are the signature of the "second-generation" nanoclusters that arise through reorganization of

Pd atoms. Pressures in the Torr range are necessary at room temperature because of the need to stabilize a steady-state high surface coverage of CO, which is not possible in vacuum. The formation of second-generation Pd nanoclusters is reversible as shown by the fact that the Pd $3d_{5/2}$ photoemission features change back to a single peak centered at 335.45 eV when CO is evacuated and high vacuum (2×10^{-9} Torr) is reached (Figure S3c).

Three peak components (I, II, and III) are needed to fit these Pd $3d_{5/2}$ spectra with different fractions that depend on the CO pressure, as shown in Figure 1b. The fitting was performed using Lorentzian asymmetric line shapes using the Casa XPS fitting program, while keeping the widths and positions fixed. The first component at 335.2 eV is observed on the clean surface at 2×10^{-10} Torr (Figure 1b1). This peak originates from the Pd atoms of the topmost and subsurface layers, whose contributions cannot be distinguished in these spectra. Starting at 3×10^{-9} Torr of CO, a second component (II) shown in green curve in Figure 1b, is observed at 335.7 eV. At CO
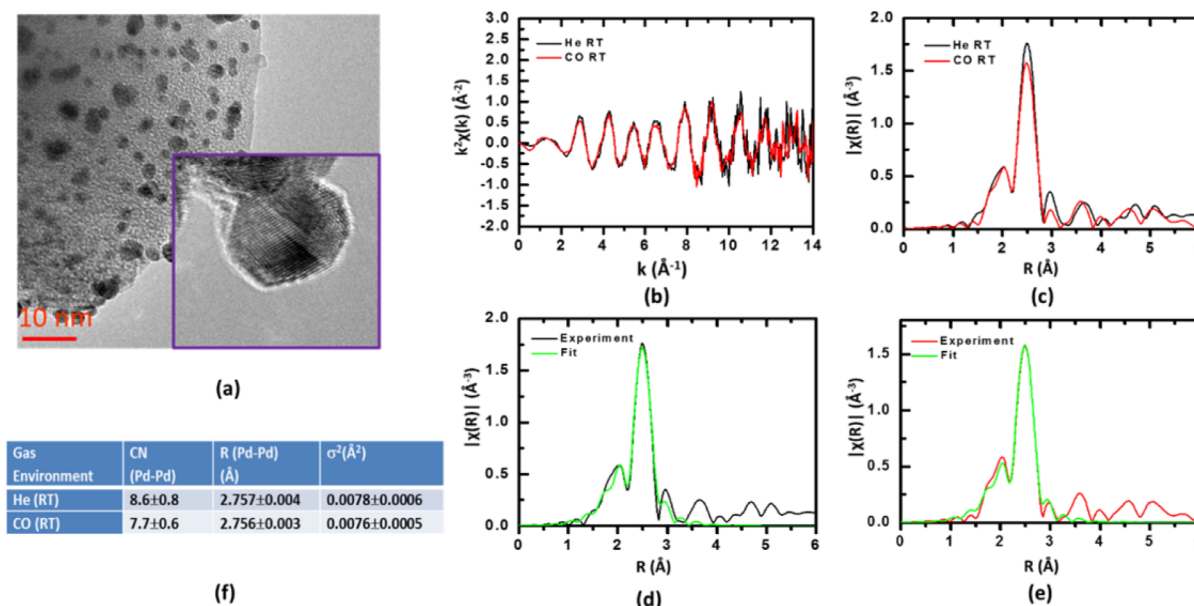
Figure 2. CN(Pd−Pd) of Pd NPs/Al$_2$O$_3$ in flowing helium and flowing 5% CO (balanced with helium) studied with in situ EXAFS. Pd NPs supported on Al$_2$O$_3$ particles were reduced to metallic Pd nanoparticles. After this reduction, 5% CO was purged and He (99.999%) was introduced. After EXAFS studies in He (99.999%), 5% CO (balanced with He) was introduced; CO was flowing through Pd NPs/Al$_2$O$_3$ at room temperature during EXAFS studies. (a) TEM images of Pd NPs/Al$_2$O$_3$ particles. (b) k-space data of Pd NPs/Al$_2$O$_3$ in flowing He (99.999%) (black line) and flowing 5% CO (red line). (c) r-space data of Pd NPs/Al$_2$O$_3$ in flowing He (99.999%) (black line) and flowing 5% CO (red line). (d) Experimental and fit r-space data of Pd K edge of Pd NPs/Al$_2$O$_3$ in flowing He (99.999%). (e) Experimental and fit r-space data of Pd K edge of Pd NPs/Al$_2$O$_3$ in flowing 5% CO. (f) CN(Pd−Pd) and R(Pd−Pd) of Pd NPs/Al$_2$O$_3$ in flowing He (99.999%) and flowing 5% CO. All data acquisitions were done when Pd NPs/Al$_2$O$_3$ were in either He (99.999%) or 5% CO at room temperature.

pressures between 3×10^{-9} and 1.5×10^{-8} Torr, CO molecules form chemisorbed structures bound to bridge and top sites on the Pd(111) surface, where the Pd atoms have a coordination number of 9.[24] Above 1.5×10^{-7} Torr, a third component (III), shown in pink, appears at 336.3 eV, 0.60 eV higher than component II. This component (III) becomes dominant at 1.5 or 5 Torr of CO (Figure 1b9). Figure 1c presents the evolution of the fractional areas of components I, II, and III of the deconvoluted Pd 3d spectra as a function of CO pressure.

To determine the coverage of CO, defined by the ratio of the number of chemisorbed CO molecules to the number of Pd atoms in the topmost layer, we calibrated the photoemission intensity ratio of C 1s/Pd 3d based on literature values.[24] In this way we obtained the CO coverage values shown in Figure 1d. The details of the calculation are given in the Methods section. As shown in Figure 1d, the coverage of CO reaches saturation at ~1.5×10^{-2} Torr. However, the fraction of component III of Pd 3d$_{5/2}$ continued to increase from ~25% at ~1.5×10^{-2} Torr to ~42% at 5 Torr (Figure 1c), although the coverage of CO remains nearly constant in this pressure range. The following EXAFS studies of Pd NPs supported on Al$_2$O$_3$ particles show the average coordination number CN(Pd−Pd) in CO gas is lower than that of the nanoparticles in pure helium, which suggests the formation of Pd atoms with lower coordination number on the surface of Pd NPs in CO gas. Thus, the new component (III) identified with AP-XPS is assigned to Pd atoms with a lower coordination number formed in CO gas.

To quantify the change in average coordination number of the Pd atoms due to the presence of CO, in situ EXAFS was performed first in a flow of He (99.999%) and then in a flowing mixture of 5% CO in He at room temperature. Because EXAFS is an ensemble technique that characterizes the entire sample

consisting of millions of nanoparticles of a catalyst, the coordination numbers obtained represent an average value. EXAFS is thus a complementary technique to electron microscopy imaging with the advantage of minimal beam damage and circumventing the limited access to a very small fraction of metal nanoparticles on the catalytic support.[25]

Because the atomic ratio of Pd atoms in the Pd NPs to the substrate, Al$_2$O$_3$ thin film grown on the NiAl crystal, is extremely low (<0.01 wt %), a high surface area catalyst (3 wt % Pd/Al$_2$O$_3$) was used for EXAFS studies. The sample was prepared by deposition-precipitation of Pd cations on 0.20 g of Al$_2$O$_3$ particles with an average size of 100−200 nm.[26] The Pd nanoparticles had an average size of about 2−3 nm (Figure 2a). Figure 2b shows the EXAFS oscillations from the Pd K-edge in a gas phase of He (99.999%) mixed with 5% CO. Data analysis of Fourier transformed spectrum shown in Figure 2b−e revealed that the coordination number (Pd−Pd) is 7.7 ± 0.6 in the CO balanced with He and 8.6 ± 0.8 for the same particles in pure He (Figure 2f). Because this measured CN(Pd−Pd) is an average of the coordination numbers of all Pd atoms in the outer layer, subsurface, and bulk of these Pd NPs with an average size of about 2−3 nm, the decrease of the CN(Pd−Pd) while Pd NPs are in CO in fact shows a decrease of coordination numbers of Pd atoms of surface region of the original Pd nanoparticles; this is because CO molecules of the gas phase first interact with Pd atoms of the surface of these Pd NPs (Figure 3).

To provide "visual" information for the change of atomic packings and the formation of second-generation nanoclusters in CO, structural models of Pd NPs in pure helium (without formation of second-generation nanoclusters) and of Pd NPs with second-generation nanoclusters in CO were considered on the basis of the size of Pd NPs examined with transmission
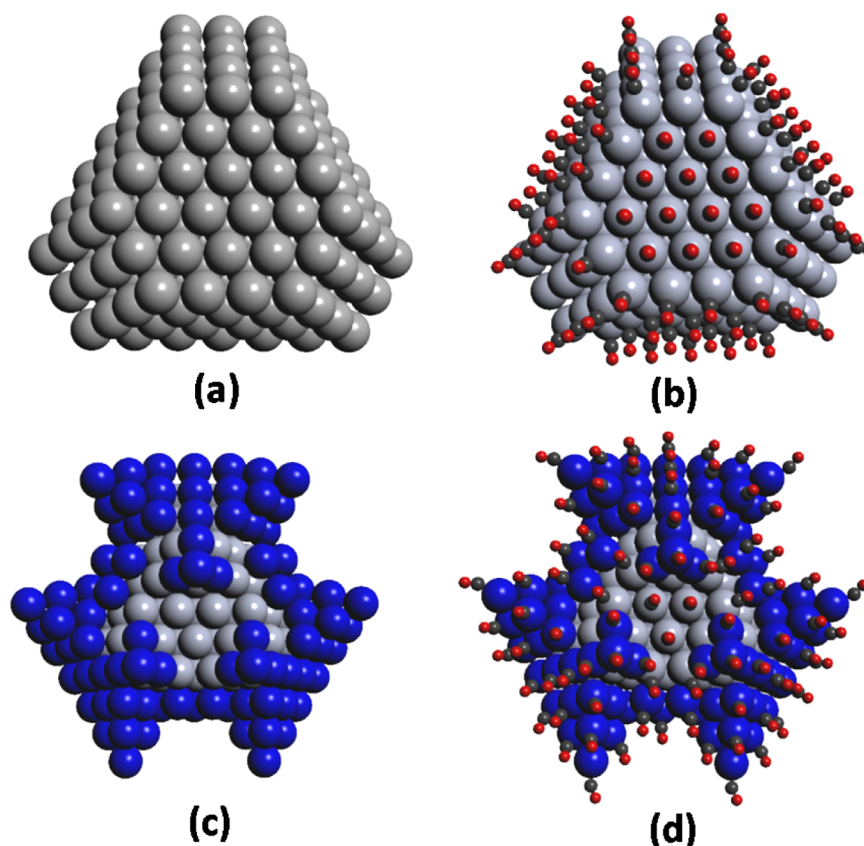
Figure 3. Presentation of the formation of second-generation nanoclusters on a metal nanoparticle in gas of a reactant at Torr pressure through reorganization of surface atoms of the metal nanoparticle. (a) Structural model of a Pd NP (166 Pd atoms); 90 atoms are on the topmost surface of this Pd NP; the exposed surfaces are mainly (111). (b) Structural model of the Pd NP of (a) with chemisorbed 81 CO molecules; the second generation nanoclusters (shown in blue) are supported on the left Pd atoms (shown in gray). (c) Structural model of second-generation Pd nanoclusters (marked with blue) formed through reorganization of the 90 Pd atoms of the topmost layer of (a); the total number of Pd atoms of the second-generation nanoclusters is 90, which is the number of the topmost atoms of Pd NP in (a). (d) Structural model of second-generation Pd nanoclusters (marked with blue) which chemisorb 81 CO molecules. (Gray, Pd atoms; blue, reorganized Pd atoms; red, oxygen atoms; black, carbon atoms.).

electron microscopy (TEM) and the average CN(Pd−Pd) in pure helium and CO/He. Figure 3a presents a structural model (top view, with the base on the Al$_2$O$_3$ support) of a Pd NP with a size of about 3 nm before exposure to CO gas. As shown in Figure S5, this nanoparticle contains 166 atoms of which 90 atoms are on the topmost surface, 33 atoms are at the interface with Al$_2$O$_3$, and 43 atoms in the subsurface and bulk. For this Pd nanoparticle, the average coordination number of all the 166 Pd atoms is 8.86, similar to that in the experiments, where CN(Pd−Pd) = 8.6 (Figure 2f) in He. In terms of the 90 atoms in the topmost surface layer, their average coordination number CN(Pd−Pd) is 7.3. Calculations of the average coordination number, CN(Pd−Pd) of the structural model discussed here can be found in Figures S5−S7. The EXAFS results show that the average coordination number of the Pd atoms, CN(Pd− Pd) in CO is decreased by 0.9 (Figure 2f).

To build a simple structural model of the metal nanoparticles in CO gas, we assume that only the topmost atomic layer of Pd atoms of the Pd nanoparticle is reorganized; the average CN(Pd−Pd) of the topmost layer of the initial Pd nanoparticle (Figure 3a) decreases from 7.3 to 6.1 in the reorganization as in the example of Figure 3c. In this model, the Pd atoms of the topmost layer form second-generation nanoclusters with a thickness of two or three atomic layers, as schematically shown in blue in Figure 3c, which occurs under CO in the Torr

pressure range (Figure 3d). As shown in Figure 3d and Figure S7b, the reorganized Pd NPs still have a portion of Pd atoms whose CN(Pd−Pd) is 8 or 9, while more than half of the reorganized 90 Pd atoms have a CN(Pd−Pd) between 3 and 6. The coexistence of Pd atoms with high coordination number, CN(Pd−Pd) = 8 or 9, and low coordination number, CN(Pd− Pd) = 3−6, is consistent with the analysis of the Pd 3d$_{5/2}$ photoemission features of AP-XPS (Figure 1c) that shows that component III corresponds to highly under-coordinated Pd atoms formed at a relatively high pressure and component II to Pd atoms with relatively high CN(Pd−Pd). It is noted that the locations of those surface Pd atoms in the visual model (Figures S6 and S7) are not necessarily the positions of Pd atoms of the formed second-generation nanoclusters. In addition, there could be other combinations of different types of under-coordinated Pd atoms that also give the measured average CN(Pd−Pd), 7.7 of Pd NPs in CO. Although this model is not meant to be an exact representation of the real new Pd nanoclusters formed in CO, it shows that component III corresponds to atoms of what we called "second-generation" nanoclusters consisting of highly under-coordinated Pd atoms, as shown in blue in Figure 3c,d and evidenced by the above in situ studies of EXAFS and AP-XPS.

To test whether nanoparticles of other transition metals could also form second-generation nanoclusters in the presence
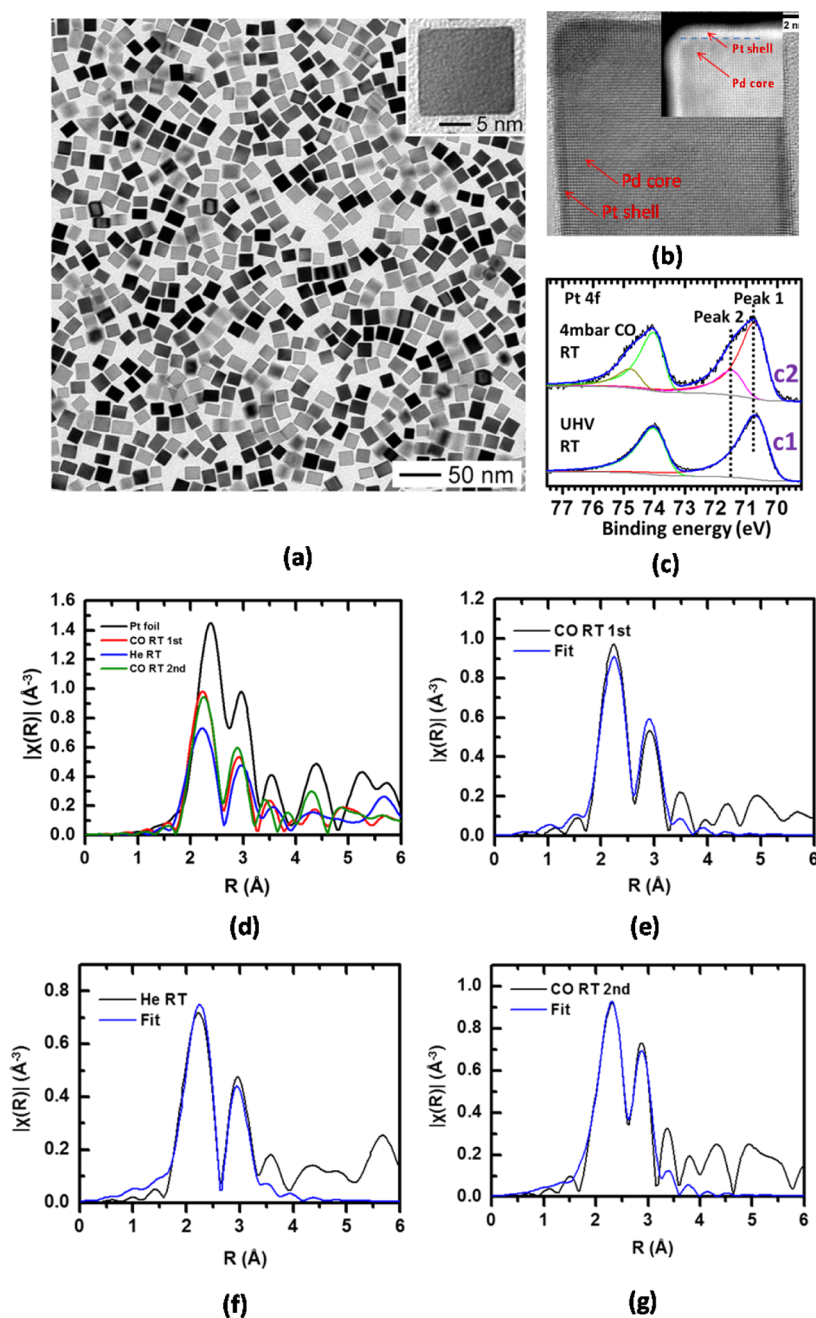
Figure 4. In situ studies of Pd@Pt$_{4L}$ core−shell nanocubes in UHV or CO gas phase by AP-XPS and EXAFS. (a) TEM image. (b) High-resolution HAADF-STEM image collected with an aberration-corrector; the Pt atoms in the shell exhibit contrast lower than Pd atoms in the core; the thickness of Pt shell is four atomic layers. (c) Pd 4f photoemission feature of Pd@Pt$_{4L}$ in UHV (panel c1) and under 4 Torr CO (panel c2); shoulders were observed in Pf 4f$_{7/2}$ and Pf 4f$_{5/2}$ under 4 Torr CO but missing for the sample in UHV. (d) r-space of Pt L$_3$ edge in CO balanced with He (red line), in pure He (blue line) upon CO was purged, and in CO balanced with He (green line) and Pt foil in a flow of pure He (black line). (e) Experimental (black line) and fitting (blue line) data of r-space of Pt L$_3$ edge in a flow of 5% CO. (f) Experimental (black line) and fitting (blue line) data of r-space of Pt L$_3$ edge in a flow of pure He. (g) Experimental (black line) and fitting (blue line) data of r-space of Pt L$_3$ edge in a flow of 5% CO.

of CO gas, we studied Pt nanoparticles on Al$_2$O$_3$/NiAl prepared using the same method as that used for Pd NPs/Al$_2$O$_3$/NiAl. The AP-XPS results in the presence of 1.5 Torr of CO (Figure S8) show indeed that the binding energies of the Pt 4f core levels also shift to higher binding energies. The Al 2s spectra in UHV and in gas phase CO, however, remains unchanged at 119.6 eV. After pumping the CO to reach UHV conditions, the high binding energy feature of Pt 4f$_{7/2}$ (red dashed line in Figure S8) downshifts to its original position

(dark dashed line), suggesting that like in the case of Pd, the surface structure of Pt NPs changes back to its original state.

To determine the coverage of CO molecules on Pt nanoparticles, we calibrated our measured photoemission intensity ratio of C 1s/Pt 4f ratios based on literature values which reported a coverage (0.5 ML) of CO on Pt(111) after exposure to 0.5 Langmuir of CO.[7,27,28] This calibration includes corrections of the different mean free paths of the Pt 4f and C 1s photoelectrons in 1.5 Torr of CO[29] (see Methods section).

The measured coverage of CO on Pt nanoparticles at 1.5 Torr is about 0.96. The Pt 4f peak in UHV (Figure S9d) was deconvoluted into contributions from Pt atoms of the topmost layer and from Pt atoms of the second and deeper layers. At a pressure of 1×10^{-8} Torr (red line in Figure S9c) and higher, the Pt atoms chemisorbing CO through top or bridge sites contribute to the peak at 71.95 eV (green spectrum, component II). Another contribution appearing at pressures of CO in the tenth of Torr and higher is the peak centered at 72.2 eV (red spectrum, component III) in Figure S9b. The atomic fractions of components I, II, and III are plotted as a function of CO pressure in Figure S9c. As can be seen, component III appears and grows at a CO pressure of 1.5×10^{-2} Torr and higher. Similar to Pd NPs (Figure 1) component III of Pt $4f7/2$ is assigned to undercoordinated metal atoms.

An important question is whether the formation of second-generation nanoclusters is related to the oxide support. To investigate it, we chose CoO as support for the Pd nanoparticles. The Pd $3d_{5/2}$ shifts from 335.3 eV in UHV to 336.2 eV in 1.5 Torr CO (Figure S10a2). After pumping out the CO gas from 1.5 Torr to 2×10^{-9} Torr, the Pd $3d_{5/2}$ peak changed to 335.3 eV (Figure S10a3) and again back to 336.2 eV after refilling the reaction cell with 1.5 Torr CO, showing the reversibility of the structural change. Therefore, we suggest that the oxide support does not play a role in the formation of second-generation metal nanoclusters.

We explored whether other reactant gases could also induce the formation of second-generation nanoclusters on metal nanoparticles. O_2, NO, and H_2 were chosen as reactants and the same AP-XPS studies of Pt $NPs/Al_2O_3/NiAl$ at different pressure of reactant gases were performed. Some similar shifts of the Pt 4f peak to high BE side were observed in reactant gases O_2 (Figure S11) and NO (Figure S12) at Torr pressure range. However, the Pt 4f peak remained the same as in UHV when in 1.5 Torr H_2 (Figure S13). No shifts of the Pt 4f peaks were observed even after heating to 100 and 200 °C in H_2. We believe that it is related to the weaker binding energy of hydrogen atoms on Pt compared to CO and NO,[2,30] and to the smaller repulsion between adsorbed hydrogen atoms, in contrast to CO or NO adsorbed on the surface.

Although the formation of second-generation nanoclusters on nanoparticles with sizes of about 3 nm was suggested with EXAFS (Figure 2), exploration of the potential occurrence of a similar phenomenon on larger nanoparticles is very challenging because EXAFS reflects the change of average coordination number of all atoms in the nanoparticles. As shown in Figure S4, the fraction of atoms of the topmost layer of a cubic NP largely decreases with the increase of its size; thus, the fraction of all metal atoms of the topmost layer in a metal nanoparticle with a size of about 10 nm is less than 10%. The actual change in coordination environment of metal atoms of surface of a 10 nm catalyst nanoparticle of metal M may not be reflected through the measurements of average coordination number of the M–M bonds in CO.

This difficulty can be overcome by using core–shell bimetallic nanoparticles consisting of a thin shell of the target metal M (shown in gray in Figure S14) and a core of another metal (shown in yellow). With the core–shell structure nanoparticles, the potential formation of second-generation nanoclusters of M through reorganization of the topmost layer should be readily reflected by a change of the average coordination number CN(M–M). For this purpose, Pd nanocubes with a dimension of about 10 nm with a Pt shell of about 1 nm thick (4 atomic layers), $Pd@Pt_{4L}$[31] were synthesized (Figure 4a,b) and studied with in situ AP-XPS and EXAFS. As shown in Figure 4c2, the shoulder at high binding energy side of Pt $4f_{7/2}$ is clearly observed at 4 Torr of CO but not in UHV (Figure 4c1). Notably, the photoemission peaks of the Pd core metal remain constant in CO and UHV. On the basis of the observation of a similar high BE shoulder of Pt $4f_{7/2}$ in Figure S9 due to the formation of nanoclusters on Pt NPs/Al_2O_3/NiAl, the result in Figure 4c2 also suggests the formation of second-generation Pt nanoclusters in the case of $Pd@Pt_{4L}$. This is consistent with the observation in EXAFS studies of $Pd@Pt_{4L}$ in two different gases, 5% CO balanced with helium and pure helium (Figure 4d). Pt L_3 edge of $Pd@Pt_{4L}$ was measured with a sequence of CO balanced with helium, pure helium, and CO balanced with pure helium. The r-space data were fitted in Figure 4e–g for the three sequential experiments. The measured coordination number, CN(Pt–Pt) of $Pd@Pt_{4L}$ at 25 °C in pure He is 10.8 (Table S1), which is the average coordination number CN(Pt–Pt) of the four layers of Pt atoms of the $Pd@Pt_{4L}$. It is consistent with the average of coordination number, CN(Pt–Pt) of the Pt shells of $Pd@Pt_{4L}$ nanocubes, 10, which is calculated with the equation,

$$CN(Pt - Pt)_{average} = \frac{nCN(Pt - Pt)_{topmost\ layer} + nCN(Pt - Pt)_{second\ layer} + nCN(Pt - Pt)_{third\ layer} + nCN(Pt - Pt)_{fourth\ layer}}{4n} = \frac{8n + 12n + 12n + 8n}{4n} = 10$$

where n is the number of Pt atom of each atomic layer. In a flowing mixture of CO balanced with He, the CN(Pt–Pt) decreases to 8.3. The decrease of coordination number suggests the formation of second-generation Pt nanoclusters in CO.

In summary, our studies of the structural evolutions of nanoparticles of metal catalysts exposed to reactant gases at Torr pressures revealed the formation of second-generation nanoclusters on the original nanoparticles, a phenomenon driven by adsorption of the reactants under pressures high enough to achieve high coverage of adsorbates despite the decreased binding arising from intermolecular repulsion. Since an industrial catalyst consists of nanoparticles different from single crystal model catalyst, here our finding suggests potential, significant structural evolution and restructuring of nanoparticles of industrial catalysts at a relatively high pressure. We expect that the report of the formation of second-generation nanoclusters from original metal nanoparticles in reactant gas at a relatively high pressure will have significant implications for correlating catalytic performance on the metal nanoparticles of a catalyst with its authentic surface structure of metal nanoparticles during catalysis.

Methods. *Preparation of Samples.* Pd NPs supported on Al_2O_3 particles (3.0 wt % Pd/Al_2O_3) were prepared with deposition precipitation with a following pretreatment in Ar and then H_2. Pd NPs supported on Al_2O_3 thin film were prepared by deposition of Pd atoms to Al_2O_3 thin film (2–3 nm thick) that was formed by oxidation of NiAl alloy in O_2. Formation of Al_2O_3 thin film (2–3 nm thick) was confirmed with identification of surface lattice of Al_2O_3 with atom-resolved images. The dimension of these Pd NPs supported on the

Al_2O_3 thin film is about 3 nm. Pd core @Pt shell nanocubes were synthesized with atomic layer-by-layer deposition of Pt on Pd nanocubes. The details of the synthesis and TEM characterization can be found from ref 31. All AP-XPS studies of this work were done on the homebuilt lab-based AP-XPS in Tao group. Reactant gases were flowing through the reaction cell designed by Tao and Nguyen.[18]

Calculation of CO Coverage on Pd or Pt Nanoparticles. Coverage of CO on surface of Pd nanoparticles is defined to the ratio of the number of the adsorbed CO molecules to Pd atoms of the topmost layer of Pd nanoparticles. It is reported that the coverage of CO on Pd(111) single crystal exposed to 8 × 10^{-9} CO for 100 s at room temperature and subsequently to restore its original UHV environment, is 0.33 based on low energy electron diffraction (LEED) studies (see ref 24). The CO coverages on Pd NPs were calculated with the following method.

The ratio of $\frac{A_{C1s}(\text{literature condition})}{A_{Pd3d}(\text{literature condition})}$ to absolute CO coverage (0.33) under the same experimental condition as reported in literature (ref 24) was taken as a calculation factor, $F_{calculation} = \frac{A_{C1s}(\text{literature condition})}{0.33 A_{Pd3d}(\text{literature condition})}$. This calculation factor was used to calculate the absolute coverage of CO adsorbed on Pd surface at other pressures. By dividing $\frac{A_{C1s}}{A_{Pd3d}}$ measured at a CO pressure at room temperature by the calculation factor, $F_{calculation}$, the absolute coverage of CO at this CO pressure is obtained, $\theta = \frac{A_{C1s}(\text{certain pressure})}{A_{Pd3d}(\text{certain pressure}) \times F_{calculation} \times F_{pressure}}$. Notably, this equation involves another factor, $F_{pressure}$. Here $F_{pressure}$ is the factor which accounts for the difference in mean free paths of photoelectrons of C 1s and Pd 3d with different kinetic energies. $F_{pressure}$ at a CO pressure is defined as $\frac{I_{p(C1s)}}{I_{0(C1s)}} / \frac{I_{p(Pd3d)}}{I_{0(Pd3d)}}$. Electron attenuation ($I_p/I_0$) of a particular electron kinetic energy in a certain pressure of gas or gas mixture can be approximated as $I_p/I_0(KE, p) = \exp\left(-\frac{z\sigma(KE)p}{kT}\right)$, where I_p is the intensity of elastically scattered photoelectrons that can be collected at aperture after they travel through the gas region (between catalyst surface and aperture) with a thickness of z at a gas pressure p; I_0 is the intensity of photoelectrons generated on surface in UHV; $\sigma(KE)$ is the electron scattering cross-section as a function of electron kinetic energy; z is the distance that electrons travel in the gas medium at temperature T. $\sigma(KE)$ can be found in literature (ref 29). During the experiment, the aperture—sample (z) distance was kept at 0.5 mm. This distance was used to calculate electron attenuation for C 1s and Pd 3d at different pressure of CO. Although $F_{pressure}$ is near to 1 and does not result in an obvious change of CO coverage, having the $F_{pressure}$ is scientifically meaningful.

With the similar method, the coverage of CO on Pt nanoparticles was calculated. The coverage of CO chemisorbed on Pt nanoparticles was calibrated with CO coverage on Pt(111) reported in literatures (refs 27 and 28).

Construction of Structural Model and the Average CN(Pd–Pd) of Original Pd NP. A structural model of Pd NP with a size of about 3 nm was built in Figure 3 and Figures S5–S7. It has 166 atoms in total. The topmost layer consists of one top facet and six side-facets. The bottom of the Pd NP bond with oxide support. The number of Pd atoms of the topmost layer of the Pd NP (the top facet and the six side facets) is 90.

The average coordination numbers of all the 166 Pd atoms of the original Pd NP is 8.86 based on EXAFS studies in helium. The average CN(Pd–Pd) of the topmost layer of Pd NP (before reorganization) is 7.30 (Figure S6). Figure S5 gives the details of the construction of the structural model and the calculation of the average CN(Pd–Pd). The consistence between the experimentally measured CN(Pd–Pd), 8.6 of Pd NPs (before reorganization) in Figure 2f and the average CN(Pd–Pd), 8.86 of the structural model (Figure S5) suggests that the structural model in Figure 3a,b (also Figure S5) is reasonable.

Structural Model and the Average CN(Pd–Pd) of a Newly Formed Pd NP in CO. A structural model of a newly formed Pd NP with a size of about 3 nm was built to represent the restructured Pd NP. Notably, this structural model is not a result of DFT calculation. It still has 166 atoms in total after the formation of the second-generation Pd nanoclusters that are marked with blue in the top panel of Figure S6. These second-generation Pd nanoclusters were formed through the 90 Pd atoms of the topmost layer described in Figure S5. The average coordination numbers of the topmost layer of the original Pd NP and of the second-generation Pd nanoclusters (marked with blue) formed in CO are 7.30 (Figure S5) and 6.10, respectively. The calculated average CN(Pd–Pd) of the structural model of the restructured Pd nanoparticles, 7.30 is consistent with the experimentally measured CN(Pd–Pd) 7.7 ± 0.6 (Figure 2f). This consistence suggests that the proposed structural model of the Pd NP consisting second-generation nanoclusters and the unrestructured base (Figures 3c and 3d) is reasonable.

Experimental and Data Analysis of EXAFS Studies of Pd NP Supported on Al_2O_3 and Pd@Pt4L. Pd K edge XAFS data of Pd NPs/Al_2O_3 and Pt L_3 edge XAFS data of Pd@Pt4L core–shell nanocubes were collected at beamline X18B, National Synchrotron Light Source, Brookhaven National Laboratory. XAFS measurements were performed in fluorescence mode using a 13-channel Ge detector. Samples were measured in the form of powder in a Clausen cell. In the measurements of Pd K edge data, the following occurred: (1) Pd NPs/Al_2O_3 was reduced in H_2 at 250 °C. EXAFS data were then collected in He at room temperature. (2) One percent CO gas was introduced and mixed with helium. XAFS data were collected at room temperature. The Pt L_3 edge XAFS data of Pd@Pt4L sample was measured in CO and pure helium at room temperature.

In the analysis of Pd K edge EXAFS data of Pd NPs/Al_2O_3, only Pd–Pd theoretical contribution was included to fit the first shell data. The passive electron reduction factor ($S_0^2 = 0.81$) was obtained by fitting Pd foil and fixed in fitting XAFS data of samples. The Pd–Pd coordination number (N), bond length (R), its mean squared disorder (σ^2), and the correction to the photoelectron energy origin (ΔE_0) were fitting variables. The fitting k range is 2.0–13.0 $Å^{-1}$ and the fitting R range were 1.6–3.0 Å. Numerical best fitting results were summarized in Figure 2f.

In the analysis of Pt L_3 edge EXAFS data of Pd@Pt4L, to decrease the uncertainties of fitting parameters and increase stability of fitting results, all EXAFS data collected at three different conditions were fitted simultaneously. The fitting model for each data contains two paths: one is Pt–Pt and the other is Pt–Pd. Considering the correlation between coordination number and bond length disorder, two strategies were tested in our fitting process. The main difference of these two strategies is that both of coordination numbers and

disorder factors are allowed to be different for data collected in CO and He in Strategy 1 while only coordination numbers could be different between CO and He data in Strategy 2.

In Strategy 1, several constrains were applied to fitting variables. These constrains are (1) ΔE_0 was constrained to be the same for both Pt−Pt and Pt−Pd paths and for all three data; (2) as shown in Figure 4d of the main text, the data collected at first (CO balanced with He) and third conditions (CO balanced with He) are quite similar. The coordination number of Pt−Pt and Pt−Pd were constrained to be the same for the two data collected in CO environment.

In strategy 2, the applied constrains are (1) ΔE_0 was constrained to be the same for both Pt−Pt and Pt−Pd paths and for all three data; (2) the disorder factor of Pt−Pt and Pt−Pd was respectively constrained to be the same for data collected in three conditions. Same fitting k range (2.5−10.3 Å^{-1}) and R range (1.7−3.3 Å) were used in both strategies.

The fitting quality of the two strategies is comparable, however, the behavior of Pt−Pt coordination number is different. Using Strategy 1, the coordination number of Pt−Pt increases from 8.3 ± 2.0 in CO to 10.8 ± 3.4 in He. On the contrary, using strategy II, the Pt−Pt coordination number in He is smaller than those in CO. Because of N-σ^2 correlation, EXAFS analysis itself could not determine which strategy is better. Independent of EXAFS analysis, according to high-resolution TEM image (Figure 4b), the four-layer thickness of Pt shell with exposed (100) surface suggests the coordination number of Pt−Pt would be about 10 (see the calculation in the main text). When combined with the TEM characterization, Strategy 1 was considered more appropriate. In addition, futting using Strategy 2 gave the CN(Pt−Pt) in pure helium as 8.3, which is quite offset from average CN(Pt−Pt), 10 of a four-layer shell with a size of about 10 nm in pure helium. Compared to Strategy 2, Strategy 1 gave CN(Pt−Pt) in pure helium as 10.8, which is closer to CN (Pt−Pt), 10 of the 10 nm Pd@Pt$_{4L}$. Table S1 lists the coordination numbers, CN(Pt−Pt) and CN(Pd−Pt), and the bond lengths of Pt−Pt and Pd−Pt obtained from in situ EXAFS studies.

ASSOCIATED CONTENT

Ⓢ Supporting Information

The Supporting Information is available free of charge on the ACS Publications website at DOI: 10.1021/acs.nanolett.6b01718.

    Characterization of Pd/Al$_2$O$_3$/NiAl, Pt NPs/Al$_2$O$_3$/NiAl, Pd NPs/CoO, Pd@Pt$_{4L}$ nanocubes in reactant gases, structural evolution of Pd atoms of as-prepared Pd NP in UHV and CO, analysis of coordination environment of Pt atoms of Pd@Pt core−shell nanocubes.(PDF)

AUTHOR INFORMATION

Corresponding Authors
*E-mail: franklin.feng.tao@ku.edu.
*E-mail: mbsalmeron@lbl.gov.

Author Contributions

F.T. designed experiments, analyzed data, and wrote and edited the paper. L.N., S.Z. and Y.T. performed experiments and analyzed data. Y.L. and A.I.F. analyzed EXAFS data. L.Z. and Y.N. synthesized metal nanocubes. Y.N. edited the paper. M.S. discussed some results and wrote and edited the paper.

Notes

The authors declare no competing financial interest.

REFERENCES

(1) Ertl, G.; Knözinger, H.; Schuth, F.; Weitkamp, J. *Handbook of Heterogeneous Catalysis*; Wiley VCH: Weinheim, 2008.

(2) Somorjai, G.; Li, Y. *Introduction to Surface Chemistry and Catalysis*; Wiley VCH: Weinheim, 2010.

(3) Behrens, M.; Studt, F.; Kasatkin, I.; Kuehl, S.; Haevecker, M.; Abild-Pedersen, F.; Zander, S.; Girgsdies, F.; Kurr, P.; Kniep, B.-L.; et al. *Science* **2012**, *336*, 893−897.

(4) Chen, M. S.; Goodman, D. W. *Science* **2004**, *306*, 252−255.

(5) Parkinson, G. S.; Novotny, Z.; Argentero, G.; Schmid, M.; Pavelec, J.; Kosak, R.; Blaha, P.; Diebold, U. *Nat. Mater.* **2013**, *12*, 724−728.

(6) Hendriksen, B. L. M.; Ackermann, M. D.; van Rijn, R.; Stoltz, D.; Popa, I.; Balmes, O.; Resta, A.; Wermeille, D.; Felici, R.; Ferrer, S.; Frenken, J. W. M. *Nat. Chem.* **2010**, *2*, 730−734.

(7) Bernasek, S. L.; Somorjai, G. A. *J. Chem. Phys.* **1974**, *60*, 4552−4556.

(8) Zhang, S.; Nguyen, L.; Liang, J.-X.; Shan, J.; Liu, J.; Frenkel, A. I.; Patlolla, A.; Huang, W.; Li, J.; Tao, F. *Nat. Commun.* **2015**, *6*, 7938.

(9) Tao, F. F.; Shan, J.-j.; Nguyen, L.; Wang, Z.; Zhang, S.; Zhang, L.; Wu, Z.; Huang, W.; Zeng, S.; Hu, P. *Nat. Commun.* **2015**, *6*, 7798.

(10) Tao, F.; Crozier, P. A. *Chem. Rev.* **2016**, *116*, 3487−3539.

(11) Zhang, S.; Luan, N.; Zhu, Y.; Zhan, S.; Tsung, C.-K.; Tao, F. *Acc. Chem. Res.* **2013**, *46*, 1731−1739.

(12) Luan, N.; Cheng, F.; Zhang, S.; Tao, F. *J. Phys. Chem. C* **2013**, *117*, 971−977.

(13) Tao, F.; Dag, S.; Wang, L.-W.; Liu, Z.; Butcher, D. R.; Bluhm, H.; Salmeron, M.; Somorjai, G. A. *Science* **2010**, *327*, 850−853.

(14) Salmeron, M.; Schlogl, R. *Surf. Sci. Rep.* **2008**, *63*, 169−199.

(15) Tao, F.; Salmeron, M. *Science* **2011**, *331*, 171−174.

(16) Tao, F.; Grass, M. E.; Zhang, Y.; Butcher, D. R.; Renzas, J. R.; Liu, Z.; Chung, J. Y.; Mun, B. S.; Salmeron, M.; Somorjai, G. A. *Science* **2008**, *322*, 932−934.

(17) Tao, F. *Chem. Commun.* **2012**, *48*, 3812−3814.

(18) Nguyen, L.; Tao, F. *Rev. Sci. Instrum.* **2016**, *87*, 064101.

(19) Frenkel, A. I. *Chem. Soc. Rev.* **2012**, *41*, 8163−8178.

(20) Yang, J. C.; Small, M. W.; Grieshaber, R. V.; Nuzzo, R. G. *Chem. Soc. Rev.* **2012**, *41*, 8179−8194.

(21) Hojrup, K. H.; Sljivancanin, Z.; Laegsgaard, E.; Besenbacher, F.; Stensgaard, I. *Surf. Sci.* **2002**, *505*, 25−38.

(22) Ogletree, D. F.; Bluhm, H.; Lebedev, G.; Fadley, C. S.; Hussain, Z.; Salmeron, M. *Rev. Sci. Instrum.* **2002**, *73*, 3872−3877.

(23) Surnev, S.; Sock, M.; Ramsey, M. G.; Netzer, F. P.; Wiklund, M.; Borg, M.; Andersen, J. N. *Surf. Sci.* **2000**, *470*, 171−185.

(24) Ohtani, H.; Van Hove, M. A.; Somorjai, G. A. *Surf. Sci.* **1987**, *187*, 372−386.

(25) Li, Y.; Zakharov, D.; Zhao, S.; Tappero, R.; Jung, U.; Elsen, A.; Baumann, P.; Nuzzo, R. G.; Stach, E. A.; Frenkel, A. I. *Nat. Commun.* **2015**, *6*, 7583.

(26) Wei, Z.; Sun, J.; Li, Y.; Datye, A. K.; Wang, Y. *Chem. Soc. Rev.* **2012**, *41*, 7994−8008.

(27) Steininger, H.; Lehwald, S.; Ibach, H. *Surf. Sci.* **1982**, *123*, 264−282.

(28) Cudok, A.; Froitzheim, H.; Schulze, M. *Phys. Rev. B: Condens. Matter Mater. Phys.* **1993**, *47*, 13682−13686.

(29) Shirai, T.; Tabata, T.; Tawara, H. *At. Data Nucl. Data Tables* **2001**, *79*, 143−184.

(30) Lin, T. H.; Somorjai, G. A. *Surf. Sci.* **1981**, *107*, 573−585.

(31) Xie, S.; Choi, S.-I.; Lu, N.; Roling, L. T.; Herron, J. A.; Zhang, L.; Park, J.; Wang, J.; Kim, M. J.; Xie, Z.; Mavrikakis, M.; Xia, Y. *Nano Lett.* **2014**, *14*, 3570−3576.